Journal of Superconductivity and Novel Magnetism (2025) 38:100
https://doi.org/10.1007/s10948-025-06902-1

RESEARCH

Crystalline, Magnetic and Optical Properties of the $CaLaSnFeO_6$ Perovskite

X. A. Velásquez Moya[1] · J. C. Rincón Fajardo[1] · S. G. Posada Barragán[2] · S. J. Niño Peña[2] · T. N. Quispe Crisolo[2] · A. Moreno Sánchez[2] · A. N. Morales Carreño[2] · C. E. Deluque Toro[3] · D. A. Landínez Téllez[1,4] · L. de Los Santos Valladares[5,6] · C. H. W. Barnes[5] · S. Holmes[7] · J. Roa-Rojas[1,4]

Received: 29 March 2024 / Accepted: 4 January 2025

Abstract

In order to obtain new materials with multifunctional properties, $CaLaSnFeO_6$ samples were synthesized by the solid reaction technique. Structural analysis was performed by X-ray diffraction technique. Rietveld refinement of the experimental data revealed that these materials crystallize in a perovskite-type monoclinic structure ($P2_1/n$, space group #14) with alternating arrangement of Fe-Sn cations along the three crystallographic axes. The strongly granular character of the surface of the material was observed by scanning electron microscopy micrographs. X-ray energy dispersive spectra exhibited a close correspondence of the composition of the samples with that expected from their stoichiometric formula. Magnetic characterization in the temperature regime $50\ K < T < 325\ K$ and applied fields up to 30 kOe suggests the occurrence of a ferromagnetic ordering with Curie temperature $T_C = 204$ K. Diffuse reflectance spectra revealed the semiconducting characteristic of the $CaLaSnFeO_6$ double perovskite with a bandgap of $E_g = 2.33$ eV. To establish the origin of the magnetic interactions, electronic structure calculations were performed in the vicinity of the Fermi level by means of the Density Functional Theory. These properties generate technological expectations in the spintronics industry for the production of information storage devices on magnetic media based on polarized spin currents such as spin valves and magnetic transistors.

Keywords Complex ordered perovskites · Crystal structure · Ferromagnetic semiconductor

✉ J. Roa-Rojas
jroar@unal.edu.co

1 Grupo de Física de Nuevos Materiales, Departamento de Física, Universidad Nacional de Colombia, 111321 Bogotá, DC, Colombia

2 Área Curricular de Física, Departamento de Física, Universidad Nacional de Colombia, 111321 Bogotá, DC, Colombia

3 Grupo de Nuevos Materiales, Facultad de Ingeniería, Universidad del Magdalena, Santa Marta, Colombia

4 Grupo de Estudios de Materiales, Departamento de Física, Universidad Nacional de Colombia, 111321 Bogotá, DC, Colombia

5 Cavendish Laboratory, Department of Physics, University of Cambridge, J.J. Thomson Ave, Cambridge CB3 0HE, UK

6 Laboratorio de Cerámicos y Nanomateriales, Facultad de Ciencias Físicas, Universidad Nacional Mayor de San Marcos, Ap. Postal 14-0149, Lima, Peru

7 Department of Electronic and Electrical Engineering, University College London, Torrington Place, London WC1E 7JE, UK

1 Introduction

The reasons why perovskite-type materials with general formula ABO_3 (A is a rare earth or alkaline earth, B is a transition metal or rare earth and O represents oxygen) have been extensively studied during the last seventy years has to do, firstly, with their chemical versatility, which allows the inclusion of various elements of the periodic table; secondly, their crystallographic characteristics, with very particular distortional effects, and third, their physicochemical complexity [1]. Because of the former, it is possible to tune different physical properties by making partial or total substitutions of the cations responsible for their composition. Structurally speaking, the unit cell can adopt cubic, tetragonal, orthorhombic, monoclinic and rhombohedral distributions [2], with octahedral coordination of the B cation with the oxygens, while A is cuboctahedrally coordinated. Because of the specific structural arrangement, BO_6 octahedra can undergo tilts and rotations that contribute to the modification of the macroscopic physical properties observed in these

Published online: 01 March 2025

materials [3]. The structural and compositional complexity of this family of ceramic materials allows the occurrence of $A_2BB'O_6$ and $AA'BB'O_6$ double perovskite structures, which facilitate the inclusion of a larger number of cations, thus enhancing the search for new physical properties, ranging from insulators, semiconductors and conductors [4, 5], in the transport of electric charge, to paramagnetic [6], ferromagnetic [7], ferrimagnetic [8], and antiferromagnetic [9] from the point of view of the arrangement of magnetic moments. As a further result, exotic properties such as colossal magnetoresistance [10], half-metallicity [11], multiferroicity [12] and ferromagnetic semiconductors [13], with incalculable technological possibilities in the spintronics industry have been discovered during the last years in the so-called complex perovskites [14].

A rather recently studied perovskite is the lanthanum orthoferrite $LaFeO_3$, which crystallizes in an orthorhombic structure belonging to the Pbnm space group (#62), composed of two pseudo-cubic centered faces with a linear arrangement of two sublattices [15]. This material is interesting because it shows antiferromagnetic ordering at room temperature, with a high Néel temperature of about 740 K and also a high thermal stability [16, 17]. On the other hand, it presents a band gap value of approximately 2.6 eV, which implies a semiconductor character [18]. Due to its properties at useful temperatures, some of the suggested applications for this type of perovskite have to do with the fabrication of photocatalysts, supercapacitors and insulating devices [19], as well as in the design of sensors for microwave dielectrics and solid electrolytes [20]. A very relevant quality presented by $LaFeO_3$, in relation to the interest of application in spintronic technology, is the multiferroic response at temperatures close to 300 K, for which its physical properties have been intensively investigated during the last 20 years [21].

On the other hand, the calcium stannate $CaSnO_3$ is another simple perovskite that also presents orthorhombic crystalline cell (Pbnm space group #62), with distortions due to the inclination of SnO_6 octahedra [22]. Due to its insulating properties, with a wide band gap (4.2—4.4 eV) [23], it offers wide applicability in the construction of gas sensors, design of transparent electrodes for voltaic cells, organic light-emitting diodes, lithium-ion batteries and photocatalysts [24]. Additionally, its optical properties are optimal for the design of phosphorescent materials applicable in signaling and light sources [25]. One of its most important applications is the design of capacitors with the ability to provide stable frequencies for decades [22]. Due to the individual characteristics of lanthanide orthoferrite and calcium stagnate ($LaFeO_3$ and $CaSnO_3$), the aim of the present work is to experimentally investigate the crystallographic distribution and microstructural features, as well as their impact on the electrical and magnetic responses of the $CaLaSnFeO_6$ material which, in principle, should constitute a double perovskite based on the two single perovskites listed above. Considering that there are no reports on the physical properties of this material, in order to infer eventual technological applications, it is important to analyze the microscopic or structural mechanisms that give rise to the macroscopic electrical and magnetic responses in this complex perovskite-type material. Density Functional Theory (DFT) calculations were implemented in order to establish the origin of interactions between electron orbitals near the Fermi level.

2 Experimental

The synthesis of the $CaLaSnFeO_6$ samples was carried out through the solid-state reaction technique, which is widely applied in the production of perovskite-type ceramics [26–28]. High purity (> 99%) Sigma-Aldrich precursor oxide powders were dried at 120 °C, weighed in stoichiometric proportions according to the formula $CaLaSnFeO_6$, ground for 3 h in an agate mortar and pressed under P = 48.13 MPa, forming disc-shaped samples of 9 mm diameter and 2.23 mm thickness. The thermal processes consisted of a first calcination treatment at 1000 °C for 24 h and a second sintering treatment at 1100 °C for 48 h, with an intermediate grinding for 30 min and pressing under the same conditions described above. Crystallographic and microstructural characterizations of the sample were performed with a PANalytical X'pert-Pro X-ray diffractometer in Bragg–Brentano configuration, with Cu-kα radiation (1.540598 Å, 45 kV, 40 mA). Data were collected over a range between 10° and 90° in 2θ, with a minimum step of 0.001° for 13 s. To determine the crystallographic parameters of the material, a Rietveld refinement was performed through the GSAS code [29]. The surface morphological analysis was performed using a Vega 3 TESCAN SB scanning electron microscope (SEM) with backscattered electron (BSE), secondary electron (SE) detectors, obtaining micrographs with magnifications of 5.0 kx, 10.0 kx and 20.0 kx. To semi-quantitatively know the surface composition of the sample, energy dispersive X-ray spectroscopy (EDS) was performed using a Bruker X-ray gun and an XFLASH 410 detector coupled to the SEM equipment. The optical response was examined by means of a Cary 5000 UV–Vis-NIR spectrometer with diffuse transmittance platform for absorbance and diffuse reflectance measurement in a wavelength regime between 200 and 2500 nm. An MPMS VersaLab Quantum Design magnetometer was used to perform magnetic susceptibility measurements as a function of temperature under zero field cooling (ZFC) and field cooled (FC) procedures, in the interval $50\ K < T < 380\ K$ and magnetization as a function of applied field in the range $-30\ kOe < H < 30\ kOe$.

3 Theoretical Calculations

DFT calculations were carried out through the Kohn–Sham equations, which were solved using Pseudopotentials and the plane-wave method available in the VASP software [30]. In the calculations, a cutoff energy of 520 eV was set to ensure an accurate representation of the electronic interactions. A dense mesh of k-points according to the Monkhorst–Pack scheme [31], with dimensions of 7 × 7x5, was implemented to sample the irreducible Brillouin zone in reciprocal space. This selection, designed specifically for the orthorhombic structure in the P21/n space group, allowed a capture of crucial information in the analysis. To accurately describe the electronic properties of the material, the Perdew-Burke-Ernzerhof parameterization, complemented with the Gradient Approximation (GGA-PBE) [32], was adopted. This combination allowed an accurate representation of the exchange correlation potential effects, enriching the understanding of the electronic structure of the system. In addition, a Hubbard potential correction (GGA + U) was applied with specific values of U = 5.3 eV for the *d* orbitals of the Fe atom. This refined inclusion allowed more realistic consideration of electron interactions in localized d orbitals. To ensure convergent and robust results, we proceeded to optimize both the atomic positions and the crystal lattice parameters. This stage was prolonged until the interatomic forces and the Pulay stress reached values below 0.001 eV/A and 0.1 kB, respectively, ensuring an accurate and stable description of the characteristics of the system under study.

4 Results and Discussion

Figure 1 shows the diffraction pattern of the $CaLaSnFeO_6$ sample showing a majority crystallographic phase obtained in the last heat treatment at 1100°. It was obtained after performing the Rieltveld refinement, that the sample $CaLaSnFeO_6$ crystallizes in a monoclinic perovskite-type primitive structure (space group $P2_1/n$), with a *180°* rotation of order 2 known as a screw axis, followed by a translation of *b/2* in the [010] direction and a slip reflection plane perpendicular to this direction. The structural parameters obtained from the Rieltveld refinement are shown in Table 1. From the structural parameters, a schematic of the unit cell of sample $CaLaSnFeO_6$ was generated, this schematic is shown in the inset of Fig. 1. It should be emphasized that the space group $P2_1/n$ is characteristic of double perovskites, understood as structures in which octahedrally coordinated cations form an ordered superstructure, so that for the composition $CaLaSnFeO_6$, Sn and Fe atoms are perfectly intercalated along the three crystallographic axes, as schematized in the inset of Fig. 1. The difference in orientation and size between the Sn-O_6 and Fe-O_6 octahedra can be clearly seen in this inset. This distortive tendency of the structure octahedra's is related to the differences between the ionic radii of the constituent atoms of the material. In Glazer's notation for octahedral distortions this structure corresponds to the system denoted $a-b+a-$. In this notation, superscript (0) represents no tilt around an axis, (+) in-phase tilt and (-) out-of-phase tilt, which means that in the $CaLaSnFeO_6$ material the octahedrons rotate out-of-phase along of the

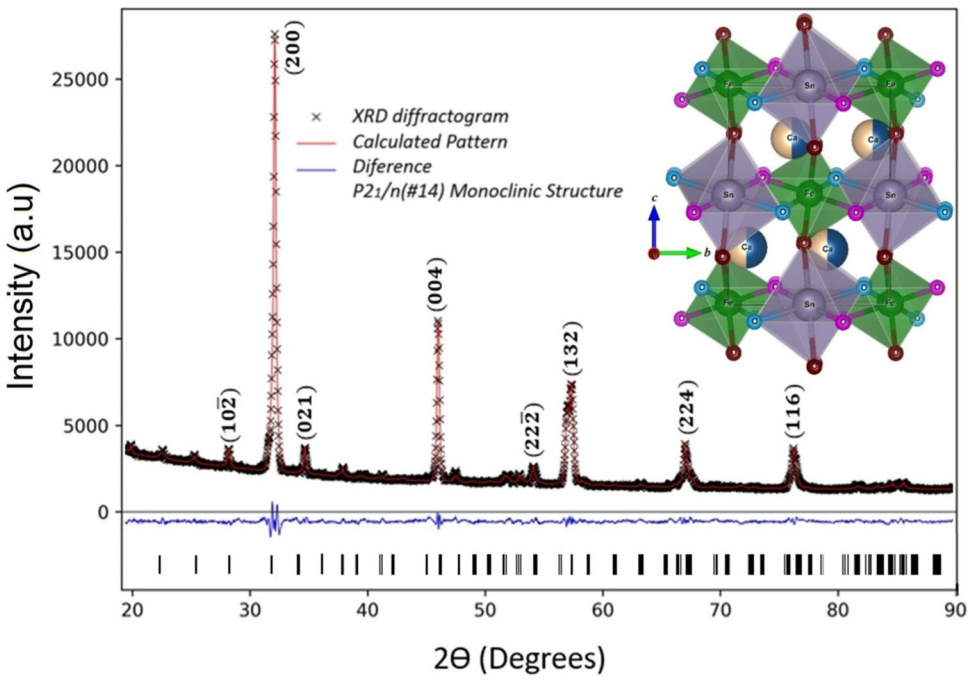

Fig. 1 Rieltveld refinement of the XRD experimental data for $CaLaSnFeO_6$ sample. Inset: Monoclinic unit cell obtained from the Rietveld refinement of XRD experimental data

Table 1 Crystallographic parameters, isotropic temperature factor and Wyckoff positions for the $CaLaSnFeO_6$ double perovskite in the monoclinic structure belonging with the $P2_1/n$ (#14) space group

Atom	*x*	*y*	*z*	Occupancy	U (Å^2)	Wyckoff Position
Ca	0.4358	0.4932	0.2321	0.5	0.0335(2)	4e
La	0.4358	0.4932	0.2321	0.5	0.0339(3)	4e
Sn	0.0000	0.5000	0.0000	1.0	0.0263(5)	2c
Fe	0.5000	0.0000	0.0000	1.0	0.0321(1)	2d
O_1	0.0620	0.3241	0.2045	2.0	0.0299(3)	4e
O_2	0.2658	0.7588	−0.0017	2.0	0.0295(5)	4e
O_3	0.7596	−0.2123	0.2481	2.0	0.0291(7)	4e
Lattice parameters	*a* (Å)	5.5838	*b* (Å)	5.5769	*c* (Å)	7.8941
Monoclinic angle		β = 89.447°		Tolerance factor		0.9275

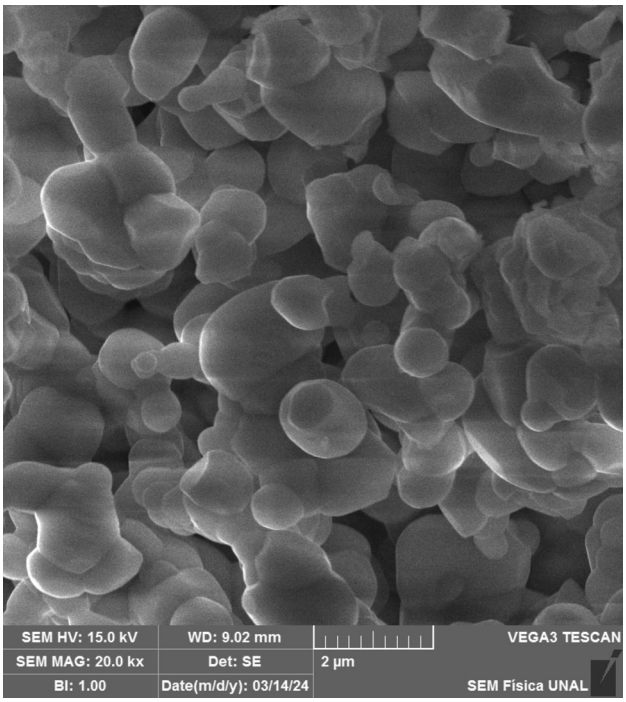

Fig. 2 Surface image for the $CaLaSnFeO_6$ sample taken at 20 k magnification with a secondary electron detector

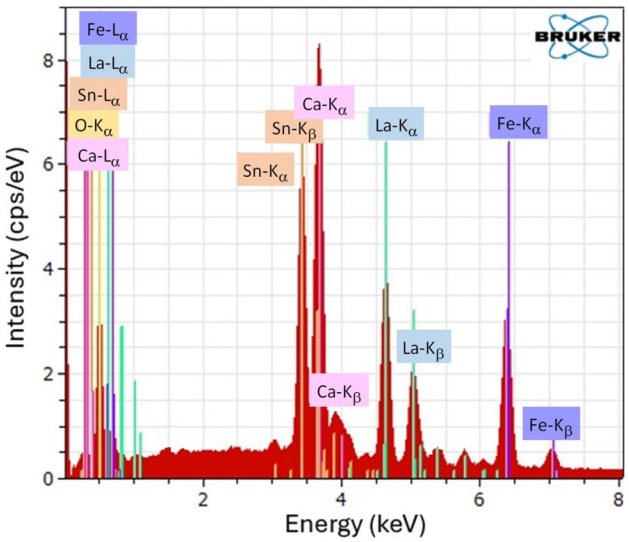

Fig. 3 EDS image for the $CaLaSnFeO_6$ material

crystallographic axes *a* and *c* in-phase along the *b* axis. In Fig. 1, the peaks indexed as (200), (004) and (224) allow to identify the octahedral in-phase tilt (*ood*) along the direction of the parameter *b*, while index (132) and (116) is related to out-of-phase displacements (*ddo*).

The octahedral distortions can be inferred from the Wyckoff positions presented in Table 1, where the difference between the locations of the O_1, O_2 and O_3 oxygens in the cell for the crystallographic positions is clear. As a consequence, two octahedral tilting angles (17.0650° and 17.4105°) take place in the structure and three different bond angles (Sn–O-Fe) occur for the three structural directions: 152.02°, 151.97° and 151.58°.

Figure 2 exemplifies the surface morphology through SEM images. The images show the formation of primary structures of irregular grains, strongly diffused, showing interconnections between them, but evidencing some boundaries leading to the formation of pores and depressions on the entire surface of the sample. The analysis of granular dimensions established the occurrence of grains with sizes varying between 0.638 µm and 1.443 µm. Meanwhile, the formation of the larger grains took place by interdiffusion of grains of sub-micrometer dimensions, as in the figure the conformation of agglomerates whose boundaries are diluted by collar structures that subsequently disappear to give rise to grains of micrometer sizes.

The experimental composition was determined the data obtained through the electron X-ray energy dispersive spectrum (EDS) used to establish the composition of the $CaLaSnFeO_6$ material produced by solid reaction method. Figure 3 shows the EDS analysis, where it is evident that there are no impurities in the material.

Table 2 Percentages by weight of each of the constituent atoms of the material determined experimentally by EDS and theoretically from the proposed stoichiometry $CaLaSnFeO_6$

Atom	Exp. wt%	Theor. wt%
Ca	9.01	8.91
La	31.11	30.90
Sn	26.59	26.41
Fe	12.48	12.42
O	20.81	21.36

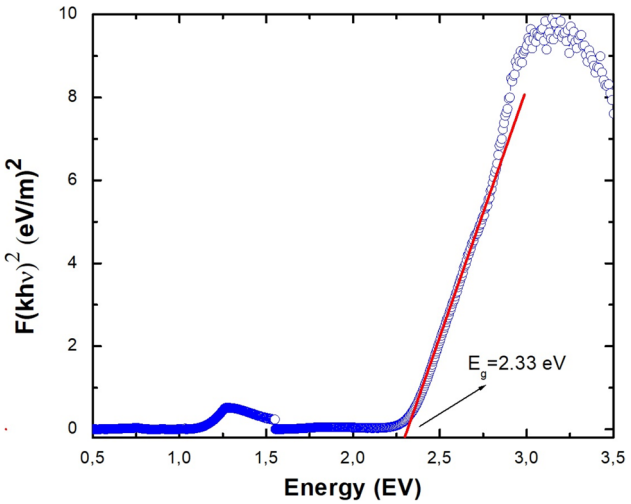

Fig. 4 Kubelka–Munk analysis for the determination of optical bandgap in the $CaLaSnFeO_6$ material by diffuse reflectance measurements

By deconvolution of the spectrum in Fig. 3, it was possible to establish a compositional coincidence of 98% between the mass values of each of the constituent atoms of the material determined experimentally and those expected from the stoichiometry of the formula $CaLaSnFeO_6$, as shown in Table 2.

Table 2 shows a small increase in the percentages of the cations while a decrease in the percentage of the anion is perceived, which occurs because oxygen has a large ionic radius and few electronic orbitals, decreasing the probability of electron scattering from the microscope beam compared to the probabilities of the cations that contain a greater number of electronic orbitals.

In order to establish the bandgap value of the $CaLaTiFeO_6$ material, wavelength-dependent diffuse reflectance measurements were performed using a UV–vis-NIR spectrophotometer. The resulting spectrum was analyzed by the Kubelka–Munk method [33], as shown in Fig. 4, where the spectrum obtained from the percentage reflectance as a function of wavelength is plotted in terms of the Kubelka–Munk function with respect to energy. This result reveals the semiconducting nature of $CaLaSnFeO_6$, with a direct bandgap of 2.33 eV ± 0.01 eV. This gap value is characteristic of semiconducting materials, such as the classic CdS (E_g = 2.42 eV) [34] and oxides such as Cu_2O (E_g = 2.17 eV) [35].

As shown in Fig. 5, magnetization measurements as a function of temperature were performed, following the ZFC and FC procedures, in the presence of magnetic field intensities of 50, 200 and 1000 Oe.

Curves in Fig. 5 show irreversible behavior with blocking temperature decreasing as the value of the applied field increases. The irreversibility characteristic of spin-glass

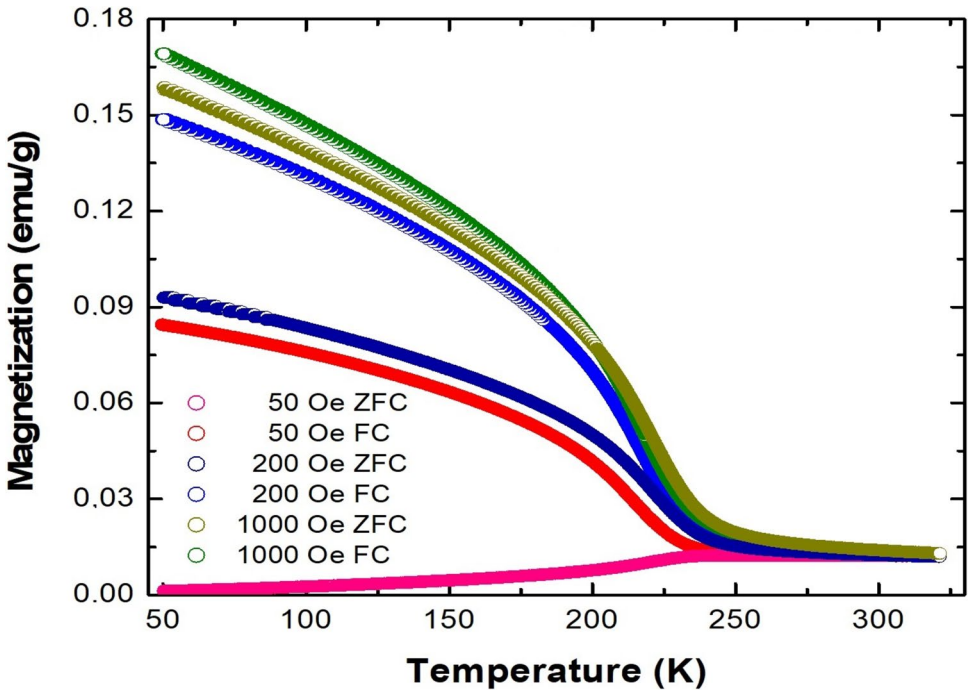

Fig. 5 Magnetization curves as a function of temperature for several applied fields on the ZFC and FC procedures

type materials [36] takes place due to magnetic disorder effects, since during the ZFC process the system of magnetic moments freezes, hindering the magnetic ordering when applying the field, while during the FC procedure the ordering takes place in a more equilibrium system. This phenomenon may be associated with cationic disorder effects, in addition to spin canting caused by octahedral distortions [37], which may introduce local magnetocrystalline anisotropies [38]. Figure 6 exemplifies an analysis of the type of ordering that takes place in this material, which was carried out by plotting the inverse of the magnetic susceptibility as a function of temperature for the measurement under application of 50 Oe.

Due to the type of nonlinear curve observed in Fig. 6 and the behavior of the magnetization in Fig. 5, ferromagnetic and antiferromagnetic ordering mechanisms were ruled out because a Curie–Weiss type fit was not applied. Instead, a fitting by means of the molecular field theory of ferrimagnetism (Eq. 1) was applied, with satisfactory results, as shown by the red line plotted [39].

$$\chi^{-1} = \frac{T-\gamma}{C} - \frac{\xi}{T-\theta} \tag{1}$$

In Eq. 1, T is the susceptibility measurement temperature, $\gamma = -715$ K represents the strength of the superexchange interaction in the Sn–O-Fe bonds of the material that decreases the ferromagnetic character, giving rise to a ferrimagnetic effect, $\xi = 1340$ Oe.mol.K/emu is a parameter related to the curvature of the inverse of the susceptibility that gives rise to the nonlinear response of $\chi(T)$, and $\theta = 12.4$ K is the Néel temperature. From this analysis, the Curie constant $C = 4.1 \pm 0.1$ emu.K/mol. Oe was obtained, corresponding to an effective magnetic

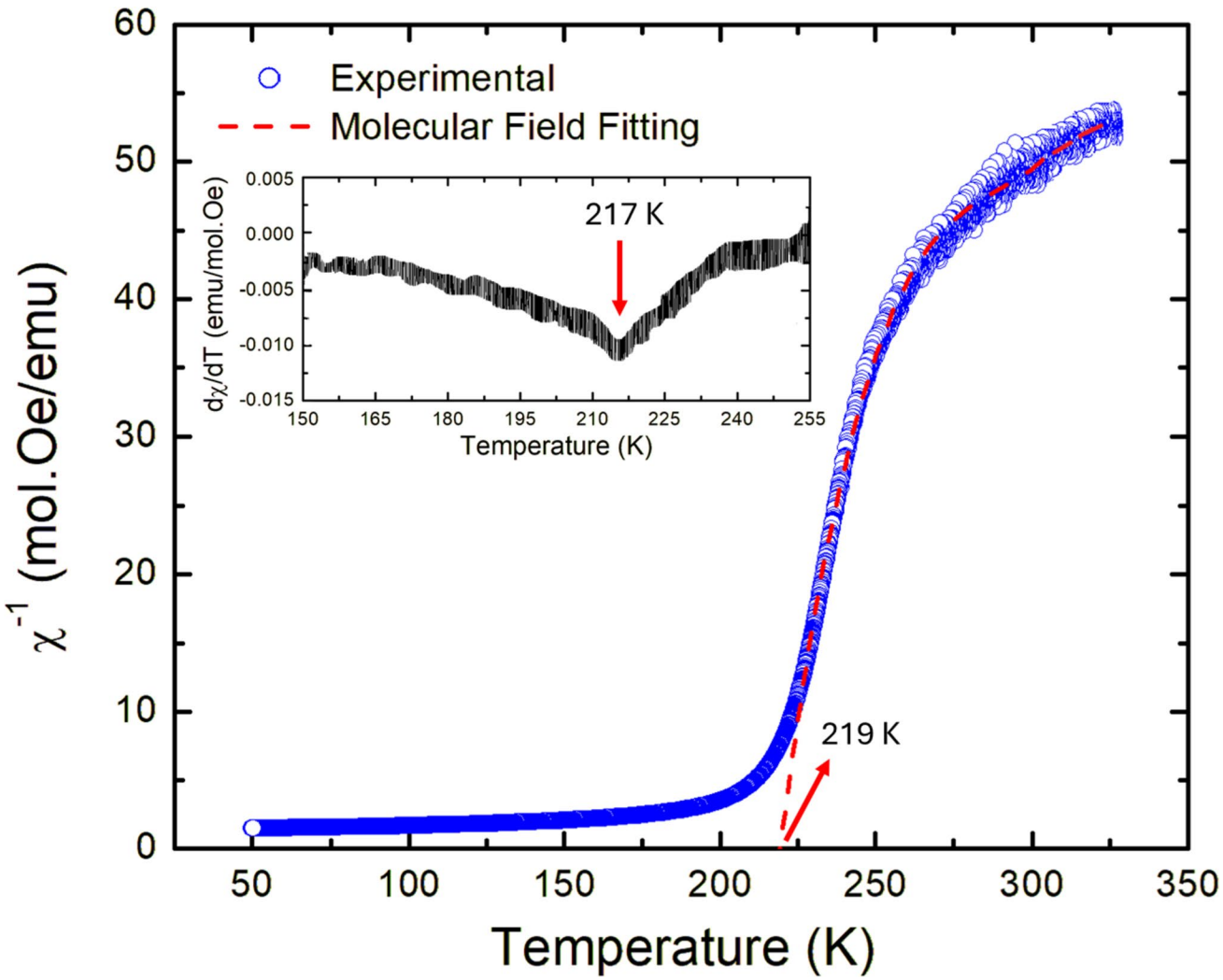

Fig. 6 Fitting the magnetic response of the $CaLaSnFeO_6$ material to the molecular field theory equation of ferrimagnetism. The inset corresponds to the derivative of the susceptibility as a function of temperature in the vicinity of the magnetic ordering temperature

moment of 5.7 μ_B. This effective magnetic moment is close to the expected value, considering that there would only be substantial contributions of Fe^{3+} (5.9 μ_B) in the $CaLaSnFeO_6$ unit cell. From the extrapolation of the fitting curve with the molecular field theory on the temperature axis in Fig. 6, the value of the Curie temperature of the ferrimagnetic ($T_c = 219$ K) is obtained, which is very close to the value obtained through the criterion of the $d\chi/dT$ curve ($T_c = 217$ K), as shown in the inset of Fig. 6.

Corroboration of the occurrence of a transition between paramagnetic and ferromagnetic states at 204 K was performed by means of the ferromagnetic hysteresis curves shown in Fig. 7.

The curves in the picture reveal a typical hysteretic response of ferromagnetic materials at temperatures of 200 K and 50 K, being essentially paramagnetic at room temperature, in agreement with the behavior observed in the magnetization response as a function of temperature (Fig. 5). Additionally, Fig. 7 shows an increase in the absolute magnetic moment, which is in agreement with the magnetization curves as a function of temperature in Fig. 5.

Band structure calculations close to the Fermi level are shown in Fig. 8 for the spin up and spin down configurations. The curves exhibit semiconductor-like features, with direct bandgap of 3.10 eV for spin up orientation and indirect bandgap of 2.56 eV for spin down polarization.

According to the scheme shown in Fig. 8, while for one spin orientation an external excitation of 3.10 eV is sufficient to promote charge carriers from the valence band to the conduction band, for the other spin polarization, in addition to an excitation greater than 2.56 eV, phonon energy is required to guarantee electric charge conduction.

The electronic analysis was complemented with calculations of the density of states, as exemplified in Fig. 9. This result suggests that at low temperatures, i.e., below 204 K, the material behaves as a ferromagnetic semiconductor, with the hybridizations between Fe-3d and O-2p orbitals for spin down polarization being responsible for the magnetic ordering that gives rise to the ferromagnetic response in the $CaLaSnFeO_6$ material. The asymmetry between the bandgaps for the two spin configurations is an imprint that takes place in this type of multifunctional materials, where the emergence of a channel for the transport not only of electric charge currents but also of spin currents is appreciated [40]. The calculated effective magnetic moment was 5.0 μ_B, which is very close to that established experimentally by molecular field theory analysis.

5 Conclusion

The solid-state reacted $CaLaSnFeO_6$ materials showed monoclinic structural phase crystallization of double perovskite type (space group $P2_1/n$, #14), which suggests the arrangement of Sn and Fe cations along the crystalline axes. The optical response at room temperature showed a semiconducting characteristic with a direct bandgap $E_g = 2.33$ eV. As the temperature decreased, magnetization curves revealed

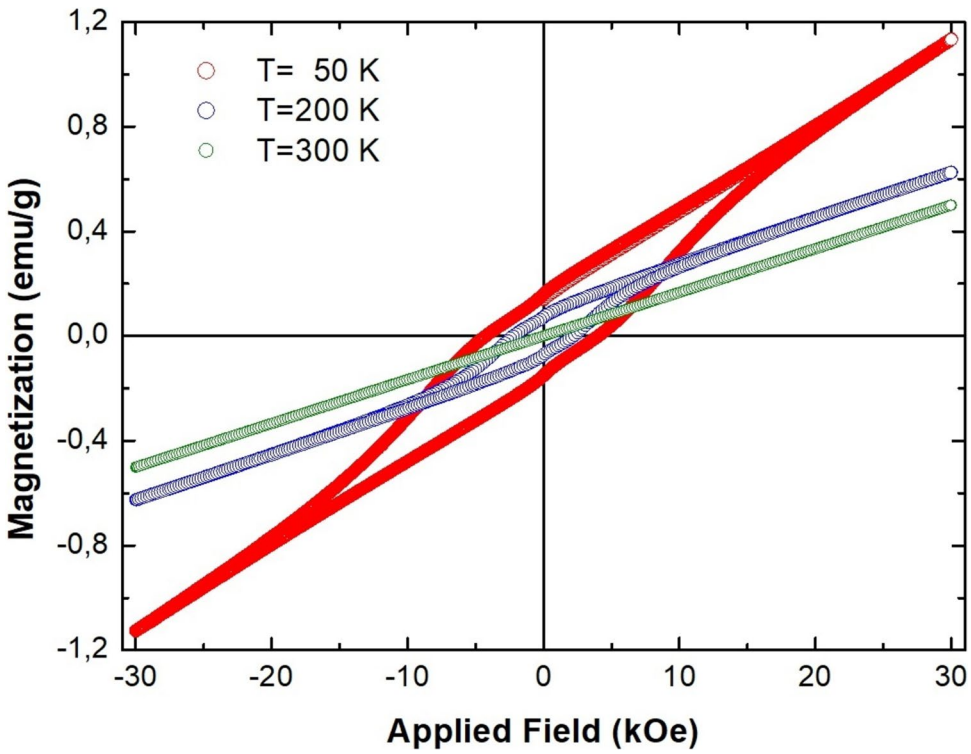

Fig. 7 Hysteresis curves of magnetization as a function of external field for the $CaLaSnFeO_6$ material

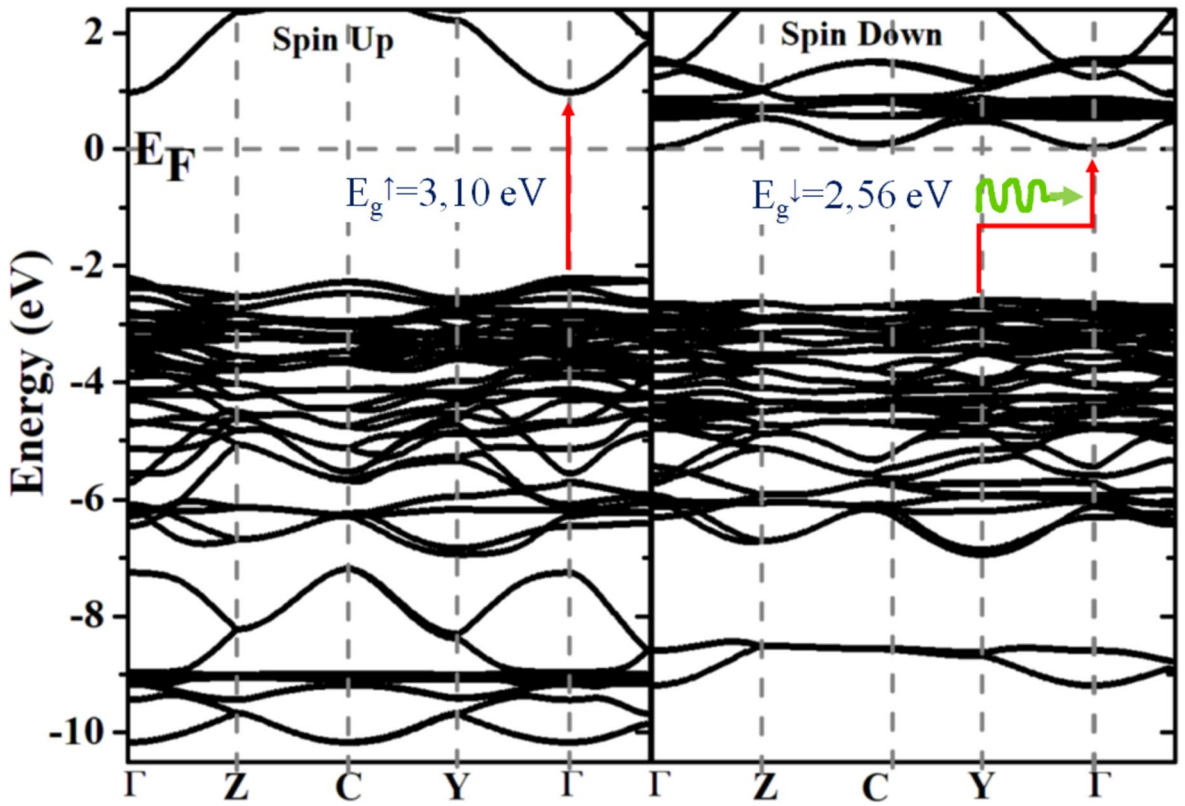

Fig. 8 Spin-polarized band structures calculated for the $CaLaSnFeO_6$ double perovskite

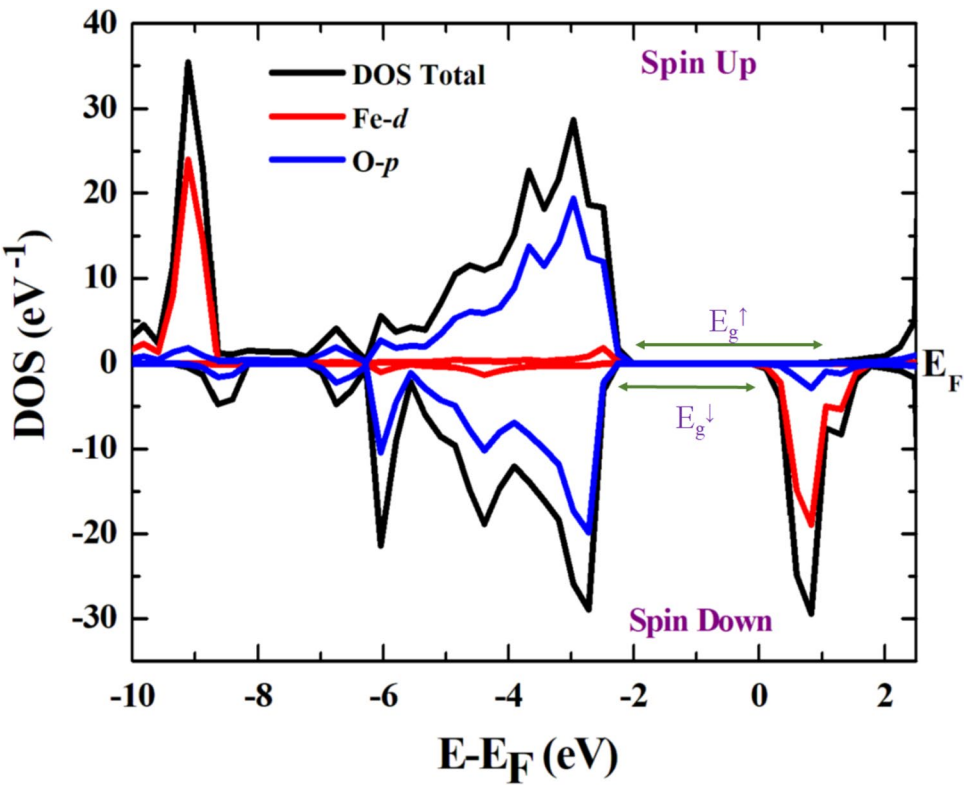

Fig. 9 Total and Fe-3d and O-2p partial density of states calculated for the up and down spin polarizations

the occurrence of a transition between paramagnetic and ferromagnetic states with a Curie temperature $T_C \approx 217$ K. Meanwhile, traces of magnetic disorder were evident in the irreversibility between the curves obtained through ZFC and FC procedures, which were associated with structural distortion effects. The electronic structure calculations in the ground state showed evidence of a semiconducting characteristic, with differences between the bandgap values for the two spin polarizations, as expected in ferromagnetic semiconductors, so it can be stated that at $T < T_C$, the material adopts a semiconducting disposition. Meanwhile, for one of the spin orientations the bandgap was direct, while for the other it was indirect. The majority contributions to the ferromagnetic semiconductor type effects are essentially from the hybridizations in the Fe-O_6 coordinations.

Acknowledgements This work was partially supported by the División de Investigación of the Universidad Nacional de Colombia – Sede Bogotá, Hermes Code 57456.

Author Contributions X.A. Velásquez Moya, J.C. Rincón Fajardo, S.G. Posada Barragán, S.J. Niño Peña, T.N. Quispe Crisolo, A. Moreno Sánchez and A.N. Morales Carreño produced the samples through the solid reaction technique and participated in the structural analysis process. C.E. Deluque Toro ran the VASP code for the calculation of the electronic properties and participated in its interpretation. D.A. Landínez Téllez coordinated and supervised the synthesis process, Rietveld refinement of the XRD data, measurements of diffuse reflectance spectroscopy and morphological and compositional characterizations. L. de Los Santos Valladares, C.H.W. Barnes and S. Holmes were responsible for magnetic characterization with their respective interpretation and revision of the final manuscript. J. Roa-Rojas is the director of the project, he proposed the new material, coordinated the experimental work, carried out the analysis of the theoretical–experimental results and wrote the final document.

Funding Open Access funding provided by Colombia Consortium.

Data Availability No datasets were generated or analysed during the current study.

Declarations

Competing Interest The authors declare no competing interests.

References

1. Hazen, R.M.: Perovskites. Sci. Am. **258**(6), 74–80 (1988)
2. Cuervo Farfán, J., Arbey Rodríguez, J., Fajardo, F., Vera López, E., Landínez Téllez, D.A., Roa-Rojas, J.: Structural properties, electric response and electronic feature of $BaSnO_3$ perovskite. Phys. B Condens. Matter. **404**, 2720–2722 (2009). https://doi.org/10.1016/j.physb.2009.06.126
3. Lufaso, M.W., Woodward, P.M.: Jahn-Teller distortions, cation ordering and octahedral tilting in perovskites. Acta Crystallogr. Sect. B Struct. Sci. **60**, 10–20 (2004). https://doi.org/10.1107/S0108768103026661
4. Vasala, S., Karppinen, M.: A2B′B″O6 perovskites: A review. Prog. Solid State Chem. **43**, 1–36 (2015). https://doi.org/10.1016/j.progsolidstchem.2014.08.001
5. Triana, C.A., Landínez Téllez, D.A., Roa-Rojas, J.: General study on the crystal, electronic and band structures, the morphological characterization, and the magnetic properties of the Sr_2DyRuO_6 complex perovskite. Mater Charact **99**, 128–141 (2015). https://doi.org/10.1016/j.matchar.2014.11.021
6. Müller, K.A.: Paramagnetic point and pair defects in oxide perovskites. J. Phys. **42**, 551–557 (1981). https://doi.org/10.1051/jphys:01981004204055100
7. Cuervo Farfán, J.A., Deluque Toro, C.E., Parra Vargas, C.A., Landínez Téllez, D.A., Roa-Rojas, J.: Experimental and theoretical determination of physical properties of $Sm_2Bi_2Fe_4O_{12}$ ferromagnetic semiconductors. J. Mater. Chem. C. **8**, 14925–14938 (2020). https://doi.org/10.1039/D0TC02935A
8. Antunes, A.B., Baibich, M.N., Gil, V., Moure, C., Allegret-Maret, V., Peña, O.: Ferro–ferrimagnetic transitions in rare-earth perovskites. J. Magn. Magn. Mater. **320**, e464–e467 (2008). https://doi.org/10.1016/j.jmmm.2008.02.085
9. Fujita, T.C., Zhang, L.F., Kawasaki, M.: Antiferromagnetic metallic state as proved by magnetotransport in epitaxially stabilized perovskite $PbRuO_3$. Phys. Rev. Mater. **4**, 031401 (2020). https://doi.org/10.1103/physrevmaterials.4.031401/figures/5/medium
10. Ramirez, A.P.: Colossal magnetoresistance. J. Phys. Condens. Matter **9**, 8171–8199 (1997). https://doi.org/10.1088/0953-8984/9/39/005
11. Bonilla, M., Landínez Téllez, D.A., Arbey Rodríguez, J., Aguiar, J.A., Roa-Rojas, J.: Study of half-metallic behavior in Sr_2CoWO_6 perovskite by ab initio DFT calculations. J. Magn. Magn. Mater. **320**, e397–e399 (2008). https://doi.org/10.1016/j.jmmm.2008.02.179
12. Fiebig, M., Lottermoser, T., Meier, D., Trassin, M.: The evolution of multiferroics. Nat. Rev. Mater. **1**, 16046 (2016). https://doi.org/10.1038/natrevmats.2016.46
13. Nieto Camacho, J.A., Cardona Vásquez, J.A., Sarmiento Santos, A., Landínez Téllez, D.A., Roa-Rojas, J.: Study of the microstructure and the optical, electrical, and magnetic feature of the $Dy_2Bi_2Fe_4O_{12}$ ferromagnetic semiconductor. J. Mater. Res. Technol. **9**, 10686–10697 (2020). https://doi.org/10.1016/j.jmrt.2020.07.073
14. Roa-Rojas, J., Deluque Toro, C.E., Gil Rebaza, A.V., Velásquez Moya, X.A., Landínez Téllez, D.A.: Spintronic Properties in Complex Perovskites: A Concordance Between Experiments and Ab-Initio Calculations. In: Engineering Materials. pp. 183–207. Springer Science and Business Media Deutschland GmbH (2022). https://doi.org/10.1007/978-3-031-07622-0_6
15. Pidburtnyi, M., Zanca, B., Coppex, C., Jimenez-Villegas, S., Thangadurai, V.: A review on perovskite-type $lafeo_3$ based

electrodes for CO_2 reduction in solid oxide electrolysis cells: Current understanding of structure-functional property relationships. Chem. Mater. **33**, 4249–4268 (2021). https://doi.org/10.1021/acs.chemmater.1c00771
16. Fossdal, A., Einarsrud, M.-A., Grande, T.: Mechanical properties of $LaFeO_3$ ceramics. J. Eur. Ceram. Soc. **25**, 927–933 (2005). https://doi.org/10.1016/j.jeurceramsoc.2004.04.009
17. Treves, D.: Studies on orthoferrites at the Weizmann institute of science. J. Appl. Phys. **36**, 1033–1039 (1965). https://doi.org/10.1063/1.1714088
18. Kanhere, P., Nisar, J., Tang, Y., Pathak, B., Ahuja, R., Zheng, J., Chen, Z.: Electronic structure, optical properties, and photocatalytic activities of $LaFeO_3$ –$NaTaO_3$ solid solution. J. Phys. Chem. C **116**, 22767–22773 (2012). https://doi.org/10.1021/jp307857h
19. Sivakumar, N., Gajendiran, J., Alsalme, A., Tashiro, K.: Structural, morphological, optical, magnetic and electrochemical behavior of solid state synthesized pure and Sr-doped $LaFeO_3$ nanoparticles. Phys. B Condens. Matter. **641**, 414086 (2022). https://doi.org/10.1016/j.physb.2022.414086
20. Khetre, S., Jadhav, H., Jagadale, P.N., Kulalb, S.R., Bamane, S.S.R.: Studies on electrical and dielectric properties of $LaFeO_3$. Adv. Appl. Sci. Res. **2**, 503–511 (2011)
21. Acharya, S., Mondal, J., Ghosh, S., Roy, S.K., Chakrabarti, P.K.: Multiferroic behavior of lanthanum orthoferrite ($LaFeO_3$). Mater. Lett. **64**, 415–418 (2010). https://doi.org/10.1016/j.matlet.2009.11.037
22. Antonio, J.E., Muñoz, H., Rosas-Huerta, J.L., Cervantes, J.M., León-Flores, J., Romero, M., Arévalo-López, E.P., Carvajal, E., Escamilla, R.: Effects of the phase transition on the structural, mechanical, electronic and vibrational properties of the $CaSnO_3$ perovskite: Study under hydrostatic pressure. J. Phys. Chem. Solids **163**, 110594 (2022). https://doi.org/10.1016/j.jpcs.2022.110594
23. Tran, M.H., Park, T., Hur, J.: Wide-bandgap CaSnO 3 perovskite as an efficient and selective deep-UV absorber for self-powered and high-performance p-i-n photodetector. ACS Appl. Mater. Interfaces **13**, 13372–13382 (2021). https://doi.org/10.1021/acsami.0c23032
24. Canimoglu, A., Garcia-Guinea, J., Karabulut, Y., Ayvacikli, M., Jorge, A., Can, N.: Catholuminescence properties of rare earth doped $CaSnO_3$ phosphor. Appl. Radiat. Isot. **99**, 138–145 (2015). https://doi.org/10.1016/j.apradiso.2015.02.026
25. Moreira, E., Barboza, C.A., Albuquerque, E.L., Fulco, U.L., Henriques, J.M., Araújo, A.I.: Vibrational and thermodynamic properties of orthorhombic $CaSnO_3$ from DFT and DFPT calculations. J. Phys. Chem. Solids **77**, 85–91 (2015). https://doi.org/10.1016/j.jpcs.2014.09.016
26. Satta, J., Casu, A., Chiriu, D., Carbonaro, C.M., Stagi, L., Ricci, P.C.: Formation mechanisms and phase stability of solid-state grown $CsPbI_3$ perovskites. Nanomaterials **11**, 1823 (2021). https://doi.org/10.3390/nano11071823
27. Contreras, V.R.E., Suesca, C.E.A., Toro, C.E.D., Téllez, D.A.L., Roa-Rojas, J.: Crystalline, ferromagnetic-semiconductor and electronic features of the terbium-based cobalt-ferrite Tb_2FeCoO_6. Ceram. Int. **47**, 14408–14417 (2021). https://doi.org/10.1016/j.ceramint.2021.02.020
28. Ginell, K.M., Horn, C., Von Dreele, R.B., Toby, B.H.: Materials for learning use of GSAS-II. Powder Diffr. **34**, 184–188 (2019). https://doi.org/10.1017/S0885715619000241
29. Blöchl, P.E.: Projector augmented-wave method. Phys. Rev. B **50**, 17953–17979 (1994). https://doi.org/10.1103/PhysRevB.50.17953
30. Kresse, G., Joubert, D.: From ultrasoft pseudopotentials to the projector augmented-wave method. Phys. Rev. B **59**, 1758–1775 (1999). https://doi.org/10.1103/PhysRevB.59.1758
31. Pack, J.D., Monkhorst, H.J.: "Special points for Brillouin-zone integrations"—a reply. Phys. Rev. B **16**, 1748–1749 (1976). https://doi.org/10.1103/PhysRevB.16.1748
32. Perdew, J.P., Wang, Y.: Accurate and simple analytic representation of the electron-gas correlation energy. Phys. Rev. B **45**, 13244–13249 (1992). https://doi.org/10.1103/PhysRevB.45.13244
33. Kubelka, P., Munk, F.: Ein Beitrag zur Optik der Farbanstriche. Z. Tech. Phys. **12**, 593–601 (1931)
34. Das, N.K., Chakrabartty, J., Farhad, S.F.U., Sen Gupta, A.K., IkballAhamed, E.M.K., Rahman, K.S., Wafi, A., Alkahtani, A.A., Matin, M.A., Amin, N.: Effect of substrate temperature on the properties of RF sputtered CdS thin films for solar cell applications. Results Phys. **17**, 103132 (2020). https://doi.org/10.1016/j.rinp.2020.103132
35. Zhang, L., McMillon, L., McNatt, J.: Gas-dependent bandgap and electrical conductivity of Cu_2O thin films. Sol. Energy Mater. Sol. Cells **108**, 230–234 (2013). https://doi.org/10.1016/j.solmat.2012.05.010
36 Li, R., Yu, L., Hu, Y.: Spin-glass irreversibility temperature and magnetic stabilization in ferromagnet/spin-glass bilayers. Phys. Status Solidi – Rapid Res Lett. **13**, 1–6 (2019). https://doi.org/10.1002/pssr.201900039
37. Manna, K., Bhadram, V.S., Elizabeth, S., Narayana, C., Anil Kumar, P.S.: Octahedral distortion induced magnetic anomalies in $LaMn_{0.5}Co_{0.5}O_3$ single crystals. J. Appl. Phys. **116**, 0–8 (2014). https://doi.org/10.1063/1.4891015
38. Nugraha, A.R., Arrasyid, E.N., Dedi, D., Nugroho, A.A.: The distorted octahedral and magnetocrystalline anisotropy of $FeMnO_3$ by stoner-wohlfarth model. Mater. Sci. Forum **1080**, 139–145 (2023). https://doi.org/10.4028/p-p876rw
39. Winkler, E, Canosa, S.B., Rivadulla, F., López-Quintela, M.A., Rivas, J., Caneiro, A., Causa, M.T, Tovar, M.: Phys. Rev. B. **80**, 104418 (2009). https://doi.org/10.1103/PhysRevB.80.104418
40. Anh, L.D., Hai, P.N., Tanaka, M.: Observation of spontaneous spin-splitting in the band structure of an n-type zinc-blende ferromagnetic semiconductor. Nat. Commun. **7**, 13810 (2016). https://doi.org/10.1038/ncomms13810